# A 5-dof Experimental Platform for Autonomous Spacecraft Rendezvous and Docking

Dae-Min Cho* Dongwon Jung† and Panagiotis Tsiotras‡

*School of Aerospace Engineering, Georgia Institute of Technology, Atlanta, GA, 30332-0150*

**In this paper we describe a new experimental facility at the School of Aerospace Engineering at Georgia Tech that will allow realistic testing of spacecraft autonomous rendezvous and docking (ARD) maneuvers. The previous 3-DOF Integrated Attitude Control System (IACS) was modified and upgraded to a new 5-DOF Spacecraft Simulator for Autonomous Rendezvous and Docking (SSARD) facility by adding two translational degrees of freedom. Integration of on-board cameras and a ceiling-mounted camera, along with 2D and 3D laser scanners will allow vision-based, autonomous rendezvous and docking research. We describe the specifications of both the upper and lower stages of the new experimental platform, as well as the supporting facilities (experimental arena, control room, air filling system). We also provide an overview of a real-time simulation/visualization environment, developed in MATLAB/VRML (Virtual Reality Modeling Language) that enables rapid prototyping, validation and testing of ARD control algorithms. Finally, we provide the details of an accurate and drift-free algorithm to calibrate attitude measurements using a single camera and a cross-shaped laser module.**

## I. Introduction

Recently, the US Air Force has identified space operations and related technology development as the most crucial factor for maintaining the current superiority of the US armed forces in the battlefield[a]. Consequently, there is an urgent need for space asset protection, inspection, and servicing. Such a need necessitates advanced automated, rendezvous and docking (ARD) capabilities.[1,2] Similarly, ARD and related technology are indispensable for the assembly of lightweight, flexible and/or modular large space structures, and for supporting a responsive space infrastructure, as envisioned by current and future space DoD missions. By the same token, NASA has recently identified ARD technology,[3–5] including servicing, refueling, and proximity operations in general, as a key ingredient for future space missions, both in low Earth orbit, as well as for the planned manned missions to the Moon and Mars[b]. The recent failure of the DART spacecraft[6] has revealed that, despite the great advances in the area of ARD technology, several technical issues still remain to be resolved.

Testing new ARD technology in a 1-$g$ environment is not an easy endeavor. Currently there are only a few major experimental facilities for testing docking strategies[c] and even fewer are available for academic research and education.[7,8] State-of-the-art experimental facilities are imperative for educating the next generation of aerospace engineers in advanced ARD operations.

*Graduate Student, Email: dcho3@gatech.edu.

†Post-doctoral Fellow, Email: dongwon.jung@gatech.edu.

‡Professor, AIAA Fellow, Email: tsiotras@gatech.edu.

[a]See the report of the "Commission to Assess United States National Security Space Management and Organization (http://space.au.af.mil/space_commission/)"

[b]In Ref. 3, a manned mission to Mars is considered, where the manned ship is refueled by fuel tankers launched in advance. In Refs. 4,5, a lunar mission is considered where the transfer vehicle is refueled in LEO by an orbiting fuel tanker.

[c]The three major demonstrators of ARD technology currently located at government labs are the NRL facility (http://www.nrl.navy.mil/content.php?P=02REVIEW207) that uses robotic arms, the NASA MSFC ARD facility (www.msfc.nasa.gov), and the JPL's recent Formation Flying Technology Laboratory (http://www.nasa.gov/centers/jpl/news/planetquest_floating_robots.html).

In this paper we summarize the efforts to establish an experimental facility that can support autonomous rendezvous and docking demonstrations and testing in an academic environment. The facility incorporates a 12 ft $\times$ 12 ft arena and a 5-dof spacecraft platform. This new 5-dof Spacecraft Simulator facility builds upon our previous experiences with the use of three-axial air-bearings for attitude control development and testing.[9–11] With the addition of two translational degrees of freedom on the previous 3-axis Integrated Attitude Control System (IACS), the new 5-dof Spacecraft Simulator for Autonomous Rendezvous and Docking (SSARD) facility allows realistic testing of spacecraft maneuvering control laws, especially during proximity operations. In conjunction with a diverse suite of sensors and actuators, the new platform enables one to conduct realistic testing of new control laws.

## II. From the 3DOF IACS to the 5DOF SSARD Facility

Starting in 2000, the Dynamics and Control Systems Laboratory at the School of Aerospace Engineering at Georgia Tech developed a series of three-axis rotational spacecraft platforms for undergraduate and graduate education and research. Details for these platforms can be found in Refs. 9–11. Several other universities have developed similar facilities. The reference by Schwartz et al[12] provides a nice overview of three-axis spacecraft experimental air-bearing facilities to date.

Testing rendezvous and docking and other similar proximity operations requires the addition of translational motion. As a result, the previous 3-dof Integrated Attitude Control System (IACS) platform was upgraded to incorporate two extra degrees of freedom, allowing translational motion of the whole platform. The entire simulator system, comprised of the IACS upper stage platform and the newly added lower stage, has been designed to levitate over a specifically constructed test arena (see discussion later on in the paper), while the upper stage is levitated above the lower stage using a three-axial air bearing. Subsequently, the spacecraft bus (upper stage) can attain five degrees of freedom: two translational degrees along the $x$ and $y$ axes, and three rotational degrees about all three axes.

Two types of air-bearings are used for frictionless operation of the 5-dof Spacecraft Simulator ARD facility: three linear air-bearing pads and a hemi-spherical air-bearing. The linear air-bearding pads make it possible to achieve almost friction-free translational motion of the entire system over a flat epoxy floor, while the hemi-spherical air-bearing is utilized to enable friction-free rotational motion of the spacecraft bus with respect to the supporting pedestal. Figure 1 illustrates the 3D CAD model of the 5-dof SSARD, while Figure 3 shows the pneumatic connection schematic of the linear air-pads and the hemi-spherical air-bearing.

### II.A. Lower Stage and Pedestal

The lower stage consists of four high-pressure air storage vessels (three external and visible in Figure 2(a) and a smaller one inside the pedestal), three linear air-bearing pads, a hemi-spherical air-bearing cup, and dedicated electronics that drive the solenoid valves for each air-bearing. The three external vessels have a total volume of 3000 in$^3$, while the internal vessel has a volume of 360 in$^3$. They are connected in series and are filled with compressed air at 3295 psi to provide air to both the linear and hemi-spherical air-bearings. Each linear air pad is able to levitate about 175 lbf load at an operating pressure of 25 psi. The maximum load of the hemi-spherical air-bearing is approximately 350-400 lbf at 80 psi air pressure, which is sufficient to support the upper stage. A series of high-pressure and low-pressure regulators and accompanying safety valves ensure that air flow is supplied continuously to all air-bearings at the appropriate pressure level. All air-bearings are either remotely controlled by the on-board computer or are manually operated via external switches. There are three different operation modes, which allow one to selectively open and close the valves for a 3-dof translational/rotational mode with heading change (only lower platform levitated), full 3-dof rotational mode (only upper platform levitated), and full 5-dof translational/rotational mode (both upper and lower platforms levitated). This provides great flexibility for the type of experiments one may conduct using the 5-dof SSARD.

The three linear air pads allow the lower stage to float on a very thin (air gap about 70-80 microns) cushion of air. The minimum air gap is dictated by the total weight of the platform and the maximum air flow rate and maximum pressure through the three linear air bearings. A smaller air gap is of course desirable in order to achieve longer levitation times, but the minimum small air gap is limited by the supporting surface

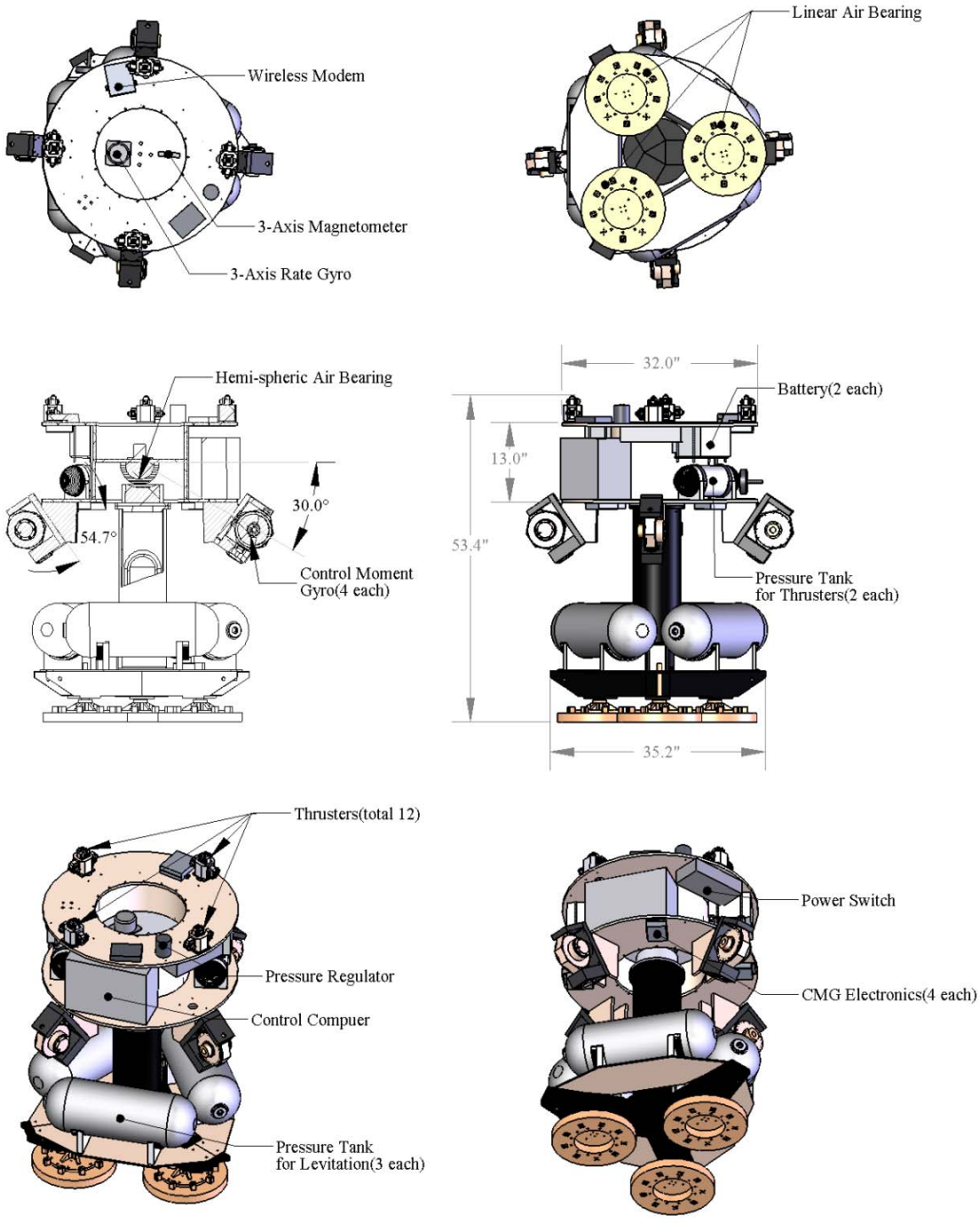


**Figure 1. 5-dof Spacecraft Simulator for Autonomous Rendezvous and Docking (SSARD) model illustration.**

undulations and other potential floor imperfections. Furthermore, very small air gaps result in increased friction between the airpads and the floor. On the other hand, a larger air gap may cause oscillations due to reduced air gap stiffness. Given the available volume of the on-board compressed air stored in the vessels, the maximum operating time was estimated to be around 30-45 minutes of continuous operation, which is deemed more than enough for our purposes. If necessary, the air flow rate can be altered manually by adjusting the output of the pressure regulators of the lower stage. The detailed schematic diagram of the pneumatic system of the lower stage is depicted in Fig. 3 with annotations of each component.

**Figure 2. Lower and upper stages of the SSARD.**

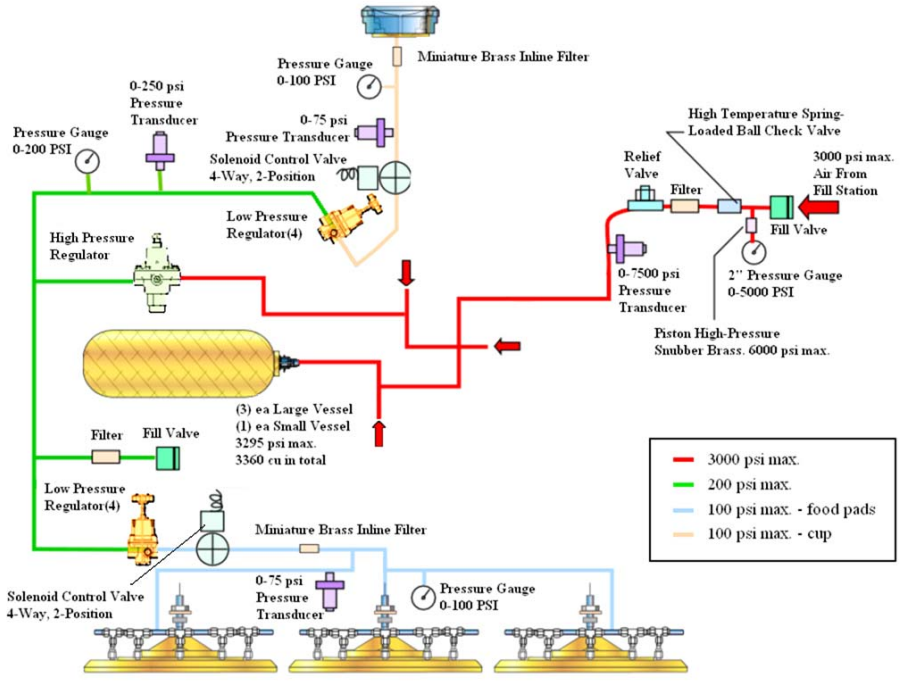


**Figure 3. Lower stage pneumatic schematic.**

## II.B. Upper Stage

The main structure of the upper stage is unchanged from the previous 3-dof IACS platform, whose operational characteristics can be found in Ref. 9. Nonetheless, several modifications have been undertaken that result in improved performance. First, a new set of thruster modules has been added to allow thrusting along all three axes. Second, the variable speed control moment gyros (VSCMGs) have been redesigned to allow

complete gimbal rotation with the help of slip rings, and the direct drive gimbal motors have been replaced by geared motors enabling tight gimbal rate control with resolution as low as 0.5 deg/sec. The servo amplifier software driving the VSCMGs has been reprogrammed for increased noise-immunity and in order to allow complete digital operation of the VSCMGs. Third, new sensors have been incorporated to allow the support of vision-based experiments.

A brief description of the main components of the upper stage is given below. More details can be found in Ref. 9.

- The upper stage spacecraft "bus" is made of a two-level brass structure that is supported on a hemispherical air bearing, allowing rotation of the upper stage with respect to the supporting pedestal about all three axes ($\pm 30$ deg about the $x$ and $y$ axes and a full rotation about the $z$ axis).
- Two 225 $in^3$ high-pressure (at 2000 psi) vessels are used to store cold-nitrogen gas for the operation of the on-board thrusters.
- A two-axis Sun/star sensor ($\pm 20$ deg vertical/horizontal range).
- A three-axis Magnetometer ($\pm 0.5$ Gauss range with resolution of 0.0006 Gauss).
- A three-axis rate gyro ($\pm 30$ deg/sec range with 0.029-deg/sec resolution about each axis)
- An inertial measurement unit (IMU), which provides independent absolute angular position ($\pm 90$ deg in roll/pitch and $\pm 180$ deg in yaw), velocity ($\pm 150$ deg/sec range with 0.073 deg/sec resolution), three-axis linear acceleration measurements ($\pm 2$ g range with 0.001 g resolution) and heading information ($\pm 1.25$ Gauss range with 0.0006 Gauss resolution).
- An on-board computer running at 750-MHz with supporting AD/DA and I/O boards.
- Two rechargeable lead-acid batteries for on-board power and associated recharging electronics.
- An ethernet wireless router (DLink DIR-625, draft 802.11n) that delivers up to 300 Mbps communication speed to the host computer.

### *II.B.1. Actuator Systems*

Unchanged from the previous configuration, the four VSCMGs are arranged in a conventional pyramid configuration and are used to provide fine attitude control. However, in order to overcome the performance limitations of the previous VSCMGs, we have incorporated slip rings (Model# AC6876 by Moog Components) and geared motors (Model# EC45 brushless with a spur gearhead GS45A by Maxon Motors). The geared motor allows very accurate gimbal rate control over the previous direct-drive motors, with a minimum gimbal rate command resolution of 0.5 deg/sec. The addition of the slip rings eliminates the rotational restriction imposed by the wires connected to the (inner) wheel motors, hence providing the capability of a full rotation of the gimbal about its axis. Subsequently, each VSCMG actuator can generate a control torque along its traverse axis regardless of its current gimbal position.

The power amplifiers that drive the VSCMGs have been redesigned to decrease their size and to allow flexibility in hardware/software maintenance. By adopting a field programmable gate array (FPGA) as the main processing unit of the VSCMG amplifiers, both the hardware and software components of the VSCMG amplifiers can now be easily reprogrammed to increase their functionality. Compared to the previous PIC microcontroller amplifiers, the current FPGA architecture allows the addition of peripherals without altering the existing circuit (extendability) and the modification of the existing control software to yield better performance (flexibility). In contrast to the previous motor control scheme, where an incremental encoder was utilized to measure the wheel speed, sensorless brushless DC (BLDC) motor control was opted for in the current implementation. The wheel speed is derived from hall sensor signals and is incorporated in the feedback loop. By this, not only we obtain accurate readings of the wheel speed with a resolution of 1 RPM, but we also avoid wheel speed noise stemming from the numerical differentiation of the encoder pulses.

The upper stage is equipped with 12 cold-gas thrusters for attitude and translational control. In order to increase the control authority of the thrusters, the number of thrusters has been increased from eight to twelve, of which four are aligned along the body $x$-axis, four are aligned along the body $y$-axis, and four are aligned along the body $z$-axis (4-4-4 configuration). The maximum thrust force generated by each thruster

is 5 lbf, and is modulated using a 10 Hz pulse width modulation (PWM) signal to make it equivalent to continuous command input. Owing to the location of the thrusters with respect to the center of rotation of the platform, the thruster forces couple the translational and the rotational motion (see Fig. 11). A thruster allocation strategy is necessary to distribute the required forces and moments to the 12 thrusters in order to provide, for instance, pure translation or pure rotation. The thruster allocation algorithm developed for the SSARD uses linear programming and is described in detail in Section V.

### *II.B.2. Vision Camera System*

A major upgrade of the upper stage has to do with the introduction of an on-board vision system. This system consists of a vision processing computer, a frame grabber board, and associated vision and laser sensors. An independent PC-104 computer (EPM-32 Cheetah from VersaLogic), is installed on the platform, and is responsible for interfacing to the vision sensors, processing the acquired vision information from the sensors, and for communicating with the main control computer. The vision computer is based on a Pentium M® 1.6-GHz high-end processor, equipped with 1-GB RAM and 4-GB compact flash drive for data and program memory, respectively. A PC-104 Meteor II-Morphis frame grabber (MOR+/2VD/J2K by Matrox Imaging) is used to grab images obtained from a standard analog CCD camera.

Several other sensors are employed for collecting information about the surroundings of the platform. An analog optical camera (TMS-730p by Pulnix) is installed on the platform to collect color images of the environment at a rate of 30 Hz. In conjunction with the frame grabber and sophisticated vision algorithms, this sensor can provide accurate information about the spacecraft orientation and position, albeit at a slower update rate. The platform is also equipped with two LADAR laser range finder sensors (URG-04LX by Hokuyo and SwissRanger SR-3000 range camera by MESA Imaging) which provide both 2D and 3D measurements. Unlike the onboard CCD camera, the two LADAR sensors are active, that is, they emit a modulated wave, and obtain range information from distant objects by calculating the time-of-flight of the reflected wave. Hence, these sensors can be utilized to collect information regardless of the ambient light conditions; they can be used under unfavorable illumination conditions, or even under complete darkness. The LADAR sensors provide highly accurate range information, allowing precise relative positioning of the spacecraft inside the experimental arena.

Both LADAR sensors have low power consumption and maintain high performance, despite their small size. The Hokuyo URG-04LX sensor, shown in Fig. 4(a), is a 2D line scan LADAR that uses an infrared laser source (wavelength 785-nm) and sweeps a 240 deg field of view with 0.36 deg resolution. The maximum detectable distance is 4 m with an accuracy $\pm 1\%$. Processing the raw data at 10 Hz, via a serial interface, this sensor provides distance and directional information of nearby objects. The SwissRanger SR-3000 LADAR camera, shown in Fig. 4(b), is a 3D laser range camera and provides 3D data sets and 2D normal intensity images with a depth map in real-time at video frame rates. The non-ambiguity range is 7.5 m with $47.5 \times 39.6$ deg field of view, which corresponds to $176 \times 144$ pixel resolution. Fifty five infrared LEDs emit amplitude modulated waves (850 nm) at 20 MHz and calculate the amplitude and phase shift of the reflected wave at each pixel to determine intensity and range information. The Hokuyo URG-04LX sensor offers direction and depth measurements at an update rate of 10 Hz. In contrast, the SwissRanger SR-3000 sensor provides 3D information without latency, yet it is lacking in resolution and its measurements need to be complemented. In a nutshell, by combining these two laser scanners (in addition to the on-board CCD camera) one can obtain highly reliable 3D information of the environment around the platform, allowing the implementation and testing of sophisticated autonomous path-planning and obstacle avoidance algorithms.

## III. Supporting Facilities

- **Epoxy Floor**

  The 5-dof SSARD platform translates on a very flat epoxy floor with the help of linear air-bearing to simulate almost friction-free conditions. A schematic of the arena is shown in Figure 8(a). The arena floor includes the operational area (156" × 168") and the stationary/parking area (40" × 58"). The surface is flat within 0.001 inches and is horizontal within a few milliradians. A cushiony rail at the outer edge of the floor protects the platform during soft collisions.


(a) Hokuyo URG-04LX. (b) SwissRanger SR-3000.

**Figure 4. On-board 2D and 3D LADAR sensors.**

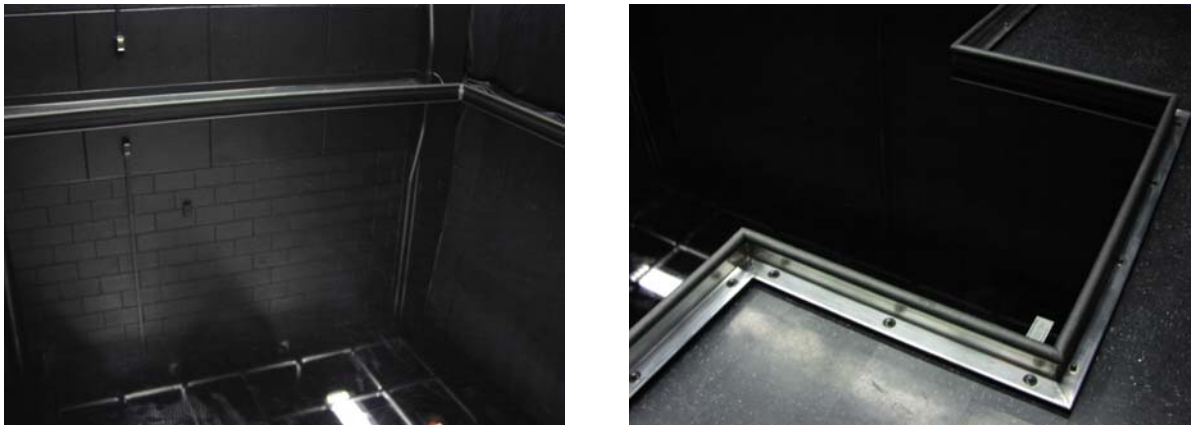

(a) Operational area. (b) Stationary/parking area.

**Figure 5. The test arena. It is made of epoxy with very tight flatness and sloping specifications.**

- **Compressed Air Filling System**

  Three high-pressure gas bottles rated up to 6000 psi are used for air storage. They are used to recharge the on-board tanks, and they can also be utilized to provide air to the platform during the experiments, if needed. A 5000 psi high pressure air compressor (90SE-5000 from Max-Air, shown in Fig. 6(a)) is utilized to fill the bottles. Additional low-pressure shop air supply is also available. Dehumidifier filters clean the shop air, and provide dry air to the 5-dof SSARD via an umbilical when the on-board tanks are depleted. The on-board gas tanks for the on-board thruster reaction control system (RCS) are charged using two additional nitrogen gas bottles (see Fig. 6).

- **Overhead Localization Facilities**

  An aluminium grid on the ceiling of the experimental area has been installed to allow mounting several equipment. Currently, a Pan/Tilt/Zoom color video camera (Sony BRC-300) is installed providing wide-angle, live-view of the experimental arena. A localizer sensor system based on four NorthStar$^{TM}$ projectors has also been installed, and is used to provide accurate measurements of the absolute position and heading of the spacecraft.

- **Control Room**

  Figure 8(b) shows a picture of the control room, which is located next to the experimental area. The experiments can be remotely operated and managed through several host computers equipped with standard software tools including Matlab/Simulink®. The computers communicate with the on-board control computer of the spacecraft platform using a wireless high-speed link. The xPC

(a) A view of the compressed air filling system.

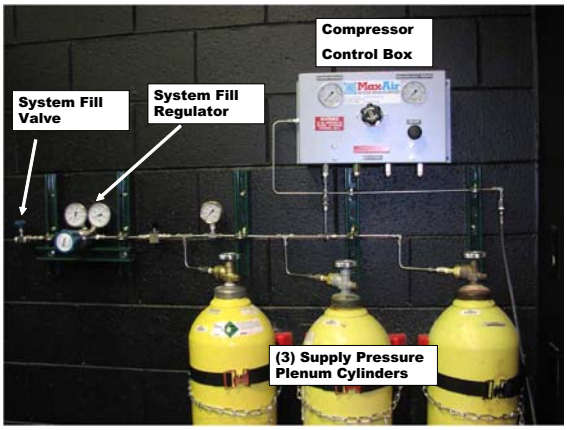


(b) The high pressure charging station.

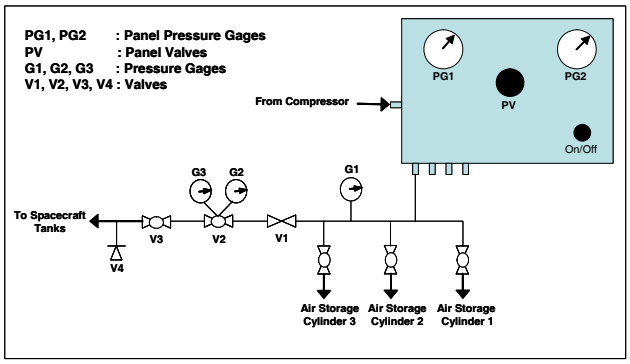


(c) A schematic diagram of the high pressure charging station.

**Figure 6. The compressed air filling system consists of a high pressure air compressor on the right of the left picture, three high-pressure gas bottles, two cold-nitrogen gas bottles, a charging station, and an air dehumidifier for the shop air.**

(a) SONY BRC-300 overview camera.

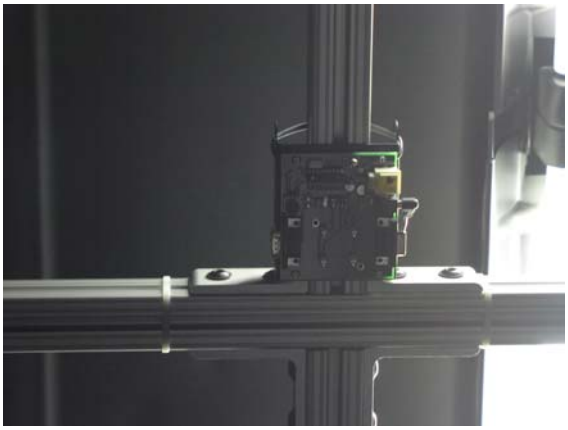

(b) NorthStar$^{TM}$ localization transmitter (four in total).

**Figure 7. Sensor suites on ceiling mounted aluminium grid.**

Target environment (with Embedded Option) from Mathworks was chosen for real-time controller implementation. Three 46" LCD overhead displays are used to display the data collected during the experiments.

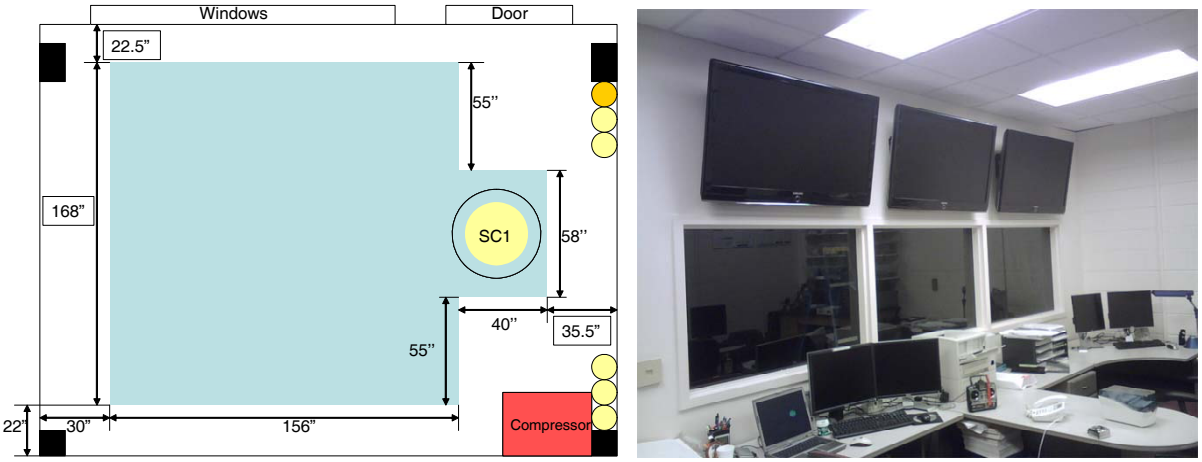


(a) Schematic of the experimental arena.

(b) Control room.

**Figure 8. Overall test facility.**

# IV. Platform Modeling

## IV.A. Model Definition

Below we derive the equations of motion of the platform. These equations are used to develop a visualization environment and also to design the control algorithms. The 5-dof SSARD consists of a number of rigid bodies: the spacecraft base platform, the lower stage, the gimbals, and the wheels. We assume no relative linear displacement between the upper and lower stages and no relative vertical displacement between the lower stage and the arena floor. In the formulation below we also allow for three-axial proof-masses, aligned to each spacecraft body axis, although these are currently not implemented on the platform. Their function is to compensate for any misalignment between the center of mass and the center of rotation of the upper stage, so that ultimately we can simulate a completely torque-free environment.

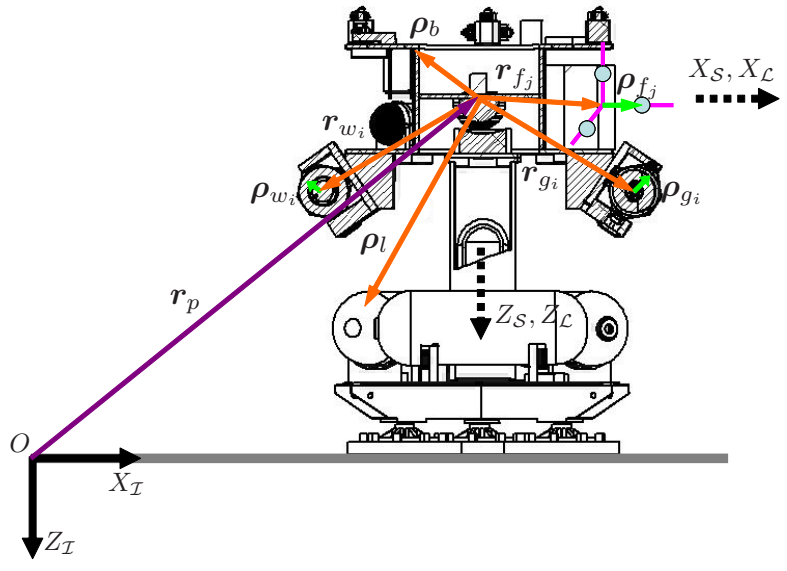


**Figure 9. A schematic for the kinetic energy derivation.**

Figure 9 shows the inertial frame ($\mathcal{I}$) located at a fixed point on the arena floor, a spacecraft platform-attached frame ($\mathcal{S}$) at the virtual pivot point of the upper platform, and a lower stage-attached frame ($\mathcal{L}$) at

the same virtual pivot point. In addition, $\boldsymbol{r}_p$ denotes the vector from the inertial origin to the virtual pivot point, $\boldsymbol{r}_*$ denotes the vector from the virtual pivot point to $* = \{g_i, w_i, f_j\}$, meaning the center of mass of each gimbal, wheel and proof-mass, respectively, $\boldsymbol{\rho}_b$ denotes the vector from the virtual pivot point to each mass element of the spacecraft platform except for $*$, and $\boldsymbol{\rho}_*$ denotes the vector from the end point of $\boldsymbol{r}_*$ to each mass element of $*$.

### IV.B. Derivation of Equations of Motion

The total kinetic energy ($T$) of the SSARD is the sum of the kinetic energy of the base platform ($\mathcal{B}$), the lower stage ($\mathcal{L}$), the gimbals ($\mathcal{G}$), the wheels ($\mathcal{W}$), and the three proof-masses. The base platform and the lower stage rotate at an angular velocity $\boldsymbol{\omega}$ and $\dot{\boldsymbol{\psi}}$ with respect to the inertial frame, respectively. The angular velocity vector of the gimbals with respect to $\mathcal{B}$ is denoted by $\dot{\boldsymbol{\gamma}}$ and the angular velocity vector of the wheels with respect to $\mathcal{G}$ is denoted by $\boldsymbol{\Omega}$. Note that $\dot{\boldsymbol{\psi}}$ is always along the $Z_{\mathcal{I}}$ axis. The kinetic energy can be easily computed as follows

$$
\begin{aligned}
T = {} & \frac{1}{2}\int_{\mathcal{B}} \frac{{}^I\mathrm{d}}{\mathrm{d}t}(\boldsymbol{r}_p + \boldsymbol{\rho}_b)\cdot\frac{{}^I\mathrm{d}}{\mathrm{d}t}(\boldsymbol{r}_p + \boldsymbol{\rho}_b)\mathrm{d}m + \frac{1}{2}\int_{\mathcal{L}} \frac{{}^I\mathrm{d}}{\mathrm{d}t}(\boldsymbol{r}_p + \boldsymbol{\rho}_l)\cdot\frac{{}^I\mathrm{d}}{\mathrm{d}t}(\boldsymbol{r}_p + \boldsymbol{\rho}_l)\mathrm{d}m \\
& + \frac{1}{2}\int_{\mathcal{G}} \frac{{}^I\mathrm{d}}{\mathrm{d}t}(\boldsymbol{r}_p + \boldsymbol{r}_g + \boldsymbol{\rho}_g)\cdot\frac{{}^I\mathrm{d}}{\mathrm{d}t}(\boldsymbol{r}_p + \boldsymbol{r}_g + \boldsymbol{\rho}_g)\mathrm{d}m + \frac{1}{2}\int_{\mathcal{W}} \frac{{}^I\mathrm{d}}{\mathrm{d}t}(\boldsymbol{r}_p + \boldsymbol{r}_w + \boldsymbol{\rho}_w)\cdot\frac{{}^I\mathrm{d}}{\mathrm{d}t}(\boldsymbol{r}_p + \boldsymbol{r}_w + \boldsymbol{\rho}_w)\mathrm{d}m \\
& + \frac{1}{2}\sum_{j=1}^{3} m_j \frac{{}^I\mathrm{d}}{\mathrm{d}t}(\boldsymbol{r}_p + \boldsymbol{\rho}_j)\cdot\frac{{}^I\mathrm{d}}{\mathrm{d}t}(\boldsymbol{r}_p + \boldsymbol{\rho}_j),
\end{aligned}
$$

where $m_j$ for $j = 1, 2, 3$ are the masses of the proof-mass actuators and where $\boldsymbol{\rho}_j = \boldsymbol{r}_{f_j} + \boldsymbol{\rho}_{f_j}$.

Expanding the kinetic energy equation and simplifying by employing the definition of the mass moment of inertia, followed by routine vector calculations, yields the following form of the total kinetic energy

$$
\begin{aligned}
T = {} & \frac{1}{2}M_t\Big(\frac{{}^I\mathrm{d}\boldsymbol{r}_p}{\mathrm{d}t}\Big)\cdot\Big(\frac{{}^I\mathrm{d}\boldsymbol{r}_p}{\mathrm{d}t}\Big) + \frac{1}{2}\boldsymbol{\omega}\cdot\boldsymbol{J}\boldsymbol{\omega} + \frac{1}{2}\dot{\boldsymbol{\psi}}\cdot\boldsymbol{I}_\ell\dot{\boldsymbol{\psi}} + \boldsymbol{\omega}\cdot\Big\{\boldsymbol{\rho}_c\times\Big(M_s\frac{{}^I\mathrm{d}\boldsymbol{r}_p}{\mathrm{d}t}\Big)\Big\} + \dot{\boldsymbol{\psi}}\cdot\Big\{\boldsymbol{\rho}_{c_\ell}\times\Big(M_\ell\frac{{}^I\mathrm{d}\boldsymbol{r}_p}{\mathrm{d}t}\Big)\Big\} \\
& + \sum_{i=1}^{4}(\boldsymbol{\omega} + \frac{1}{2}\dot{\boldsymbol{\gamma}}_i)\cdot\boldsymbol{I}_{g_i}\dot{\boldsymbol{\gamma}}_i + \sum_{i=1}^{4}(\boldsymbol{\omega} + \frac{1}{2}\dot{\boldsymbol{\gamma}}_i + \frac{1}{2}\boldsymbol{\Omega}_i)\cdot\boldsymbol{I}_{w_i}(\dot{\boldsymbol{\gamma}}_i + \boldsymbol{\Omega}_i) + \frac{1}{2}\sum_{j=1}^{3} m_j\Big(\frac{{}^S\mathrm{d}\boldsymbol{u}_j}{\mathrm{d}t}\Big)\cdot\Big(\frac{{}^S\mathrm{d}\boldsymbol{u}_j}{\mathrm{d}t}\Big) \\
& + \sum_{j=1}^{3} m_j\Big(\frac{{}^I\mathrm{d}\boldsymbol{r}_p}{\mathrm{d}t}\Big)\cdot\Big(\frac{{}^S\mathrm{d}\boldsymbol{u}_j}{\mathrm{d}t}\Big) + \boldsymbol{\omega}\cdot\sum_{j=1}^{3} m_j\Big(\boldsymbol{r}_{f_j}\times\frac{{}^S\mathrm{d}\boldsymbol{u}_j}{\mathrm{d}t}\Big),
\end{aligned}
$$

where $M_s$ is the mass of the spacecraft platform (upper stage), $M_\ell$ is the mass of the lower stage, $M_t = M_s + M_\ell$, $\boldsymbol{J}$ is the mass moment of inertia of the spacecraft platform with respect to the virtual pivot point, $\boldsymbol{I}_\ell$ is the mass moment of inertia of the lower stage with respect to the virtual pivot point, $\boldsymbol{I}_{w_i}$ is the mass moment of inertia of each wheel with respect to the virtual pivot point, and $\boldsymbol{I}_{g_i}$ is the mass moment of inertia of each gimbal (without the wheel) with respect to the virtual pivot point. In addition, $\boldsymbol{u}_j$ denotes the proof-mass position control input (equal to $\boldsymbol{\rho}_{f_j}$), and $\boldsymbol{\rho}_c$ is the vector from the virtual pivot point to the center of mass of the spacecraft platform, and $\boldsymbol{\rho}_{c_\ell}$ is the vector from the virtual pivot point to the center of mass of the lower stage.

The potential energy can be easily derived from Fig. 10. We assume that the center of mass of the lower stage remains at a constant height because the depleted air mass from onboard tanks during the operation is negligible compared to the lower stage mass. Hence, for simplicity, we select the center of mass of the lower stage as the datum. The potential energy is then given by

$$
V = M_s\,\boldsymbol{g}\cdot(\boldsymbol{\rho}_{c_\ell} - \boldsymbol{\rho}_c),
$$

where $\boldsymbol{g}$ denotes the gravitational acceleration. The SSARD is equipped with a set of thrusters generating

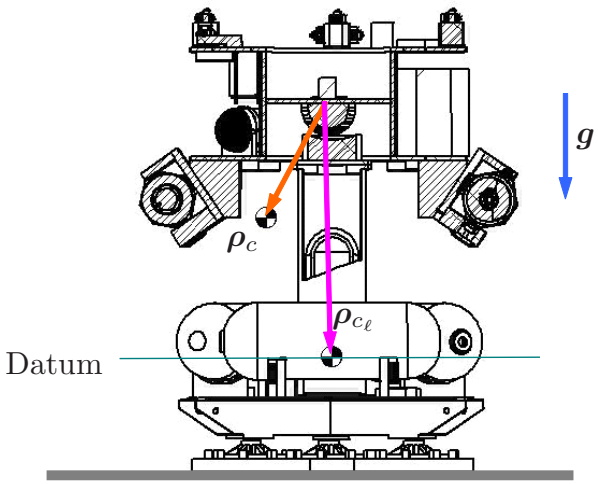


**Figure 10. Schematic for potential energy calculations.**

non-conservative forces on the platform. The force and torque vectors are given by

$$\mathbf{F}_T = \sum_{k=1}^{4} \sum_{\star} \boldsymbol{f}_{k\star},$$

$$\mathbf{M}_T = \sum_{k=1}^{4} (\boldsymbol{l}_k \times \sum_{\star} \boldsymbol{f}_{k\star}),$$

where $\mathbf{F}_T$ is the resultant thruster force and $\mathbf{M}_T$ is the resultant thruster torque, and $\star = \{p, c, n\}$. Note that the assumption that there is no vertical relative movement between the lower stage and the floor results in the holonomic constraint $\dot{Z}_{\mathcal{I}} = 0$.

The Euler-Lagrange equations yield the equations of motion for the SSARD. The Euler-Lagrange equations can be further simplified via Jacobi identity[d] and the final equations of motion of the SSARD take the form given below

$$\begin{aligned}
&\boldsymbol{J}\dot{\boldsymbol{\omega}} + \frac{{}^{S}d\boldsymbol{J}}{\mathrm{d}t}\boldsymbol{\omega} + \frac{{}^{S}\mathrm{d}\boldsymbol{\rho}_c}{\mathrm{d}t} \times \Big(M_s \frac{{}^{I}\mathrm{d}\boldsymbol{r}_p}{\mathrm{d}t}\Big) + \boldsymbol{\rho}_c \times \Big(M_s \frac{{}^{I}\mathrm{d}^2\boldsymbol{r}_p}{\mathrm{d}t^2}\Big) + \boldsymbol{\omega} \times \Big\{\boldsymbol{J}\boldsymbol{\omega} + \boldsymbol{\rho}_c \times \Big(M_s \frac{{}^{I}\mathrm{d}\boldsymbol{r}_p}{\mathrm{d}t}\Big) + \sum_{j=1}^{3} m_j \Big(\boldsymbol{r}_{f_j} \times \frac{{}^{S}\mathrm{d}\boldsymbol{u}_j}{\mathrm{d}t}\Big)\Big\} \\
&\quad + \sum_{i=1}^{4} \Big[\boldsymbol{I}_{c_i}\ddot{\boldsymbol{\gamma}}_i + \boldsymbol{I}_{w_i}\dot{\boldsymbol{\Omega}}_i + \boldsymbol{I}_{c_i}(\boldsymbol{\omega} \times \dot{\boldsymbol{\gamma}}_i) + \boldsymbol{I}_{w_i}\{(\boldsymbol{\omega} + \dot{\boldsymbol{\gamma}}_i) \times \boldsymbol{\Omega}_i\}\Big] + \sum_{j=1}^{3} m_j \Big[\boldsymbol{r}_{f_j} \times \Big(\frac{{}^{S}\mathrm{d}^2\boldsymbol{u}_j}{\mathrm{d}t^2} + \boldsymbol{\omega} \times \frac{{}^{S}\mathrm{d}\boldsymbol{u}_j}{\mathrm{d}t}\Big)\Big] \\
&\qquad - \boldsymbol{\rho}_c \times (M_s\boldsymbol{g}) = \sum_{k=1}^{4} (\boldsymbol{l}_k \times \sum_{\star} \boldsymbol{f}_{k\star}), \qquad (1)
\end{aligned}$$

$$\begin{aligned}
&M_t \frac{{}^{I}\mathrm{d}^2\boldsymbol{r}_p}{\mathrm{d}t^2} + M_s\Big\{\dot{\boldsymbol{\omega}} \times \boldsymbol{\rho}_c + \boldsymbol{\omega} \times \Big(\frac{{}^{S}\mathrm{d}\boldsymbol{\rho}_c}{\mathrm{d}t} + \boldsymbol{\omega} \times \boldsymbol{\rho}_c\Big)\Big\} + M_l\{\ddot{\boldsymbol{\psi}} \times \boldsymbol{\rho}_{c_\ell} + \dot{\boldsymbol{\psi}} \times (\dot{\boldsymbol{\psi}} \times \boldsymbol{\rho}_{c_\ell})\} \\
&\quad + \sum_{j=1}^{3} m_j \Big(\frac{{}^{S}\mathrm{d}^2\boldsymbol{u}_j}{\mathrm{d}t^2} + \boldsymbol{\omega} \times \frac{{}^{S}\mathrm{d}\boldsymbol{u}_j}{\mathrm{d}t}\Big) = \sum_{k=1}^{4} \sum_{\star} \boldsymbol{f}_{k\star}, \qquad (2)
\end{aligned}$$

[d] $\boldsymbol{A} \times (\boldsymbol{B} \times \boldsymbol{C}) + \boldsymbol{B} \times (\boldsymbol{C} \times \boldsymbol{A}) + \boldsymbol{C} \times (\boldsymbol{A} \times \boldsymbol{B}) = \boldsymbol{0}$.

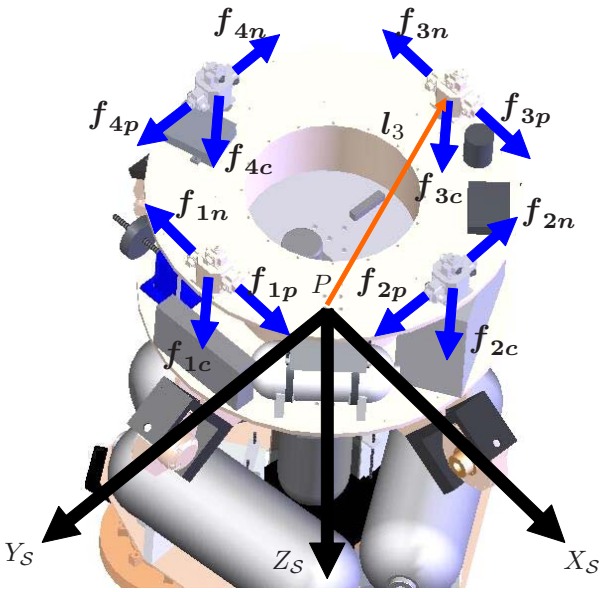


**Figure 11. Thruster force definition.**

$$\dot{Z}_{\mathcal{I}} = 0. \tag{3}$$

Equations (1), (2) and (3) form the rotational, translational and constraint equations of motion of the SSARD, respectively.

### IV.C. Simulation/Visualization Environment

For simulation and verification purposes, we ported the derived equations of motion into a Matlab/Simulink dynamics model. We adopted Matlab's Virtual Reality Toolbox for 3D visualization. Using the standard Virtual Reality Modeling Language (VRML), high-fidelity real-time virtual reality simulation is enabled by the code generated using Matlab's Real-Time Workshop (RTW) and a third-party C/C++ compiler. Later on, we plan to interface the VRML model with the actual SSARD. This will allow interaction with the SSARD in real-time via a Simulink-based external mode.

The VRML visualization tool supports a variety of views for the spacecraft and helps checking the spacecraft's state during its motion. Figure 12 depicts the developed simulation/visualization environment. We expect that this tool will substantially reduce the time required for control algorithm design, testing and validation for the SSARD.

## V. Thruster Allocation Strategy

In this section we describe a simple, yet effective, solution to the control distribution problem using a set of thrusters for rotational and translation control of the SSARD. This is referred to as the control allocation problem, for which several algorithms are available in the literature.[13,14] For the SSARD, none of the thruster force directions pass through the center of rotation. In addition, no force should be commanded along the inertial $z$-axis to maintain good contact between the upper and lower stages. As a result, the thruster allocation problem for the SSARD is somewhat more involved.

The upper stage of the SSARD is equipped with 12 thrusters, with four thrusters aligned along each of the three body axes. Due to the location of each thruster with respect to the center of rotation, firing each thruster causes not only translational motion but also coupled rotational motion. Hence, when one intends to simulate pure translational motion of the SSARD, for instance, special care is needed to compensate for the additional rotational torque. Subsequently, additional thruster firing is required to compensate for the unwanted torque components. Below we outline the thruster allocation strategy used in the SSARD, based

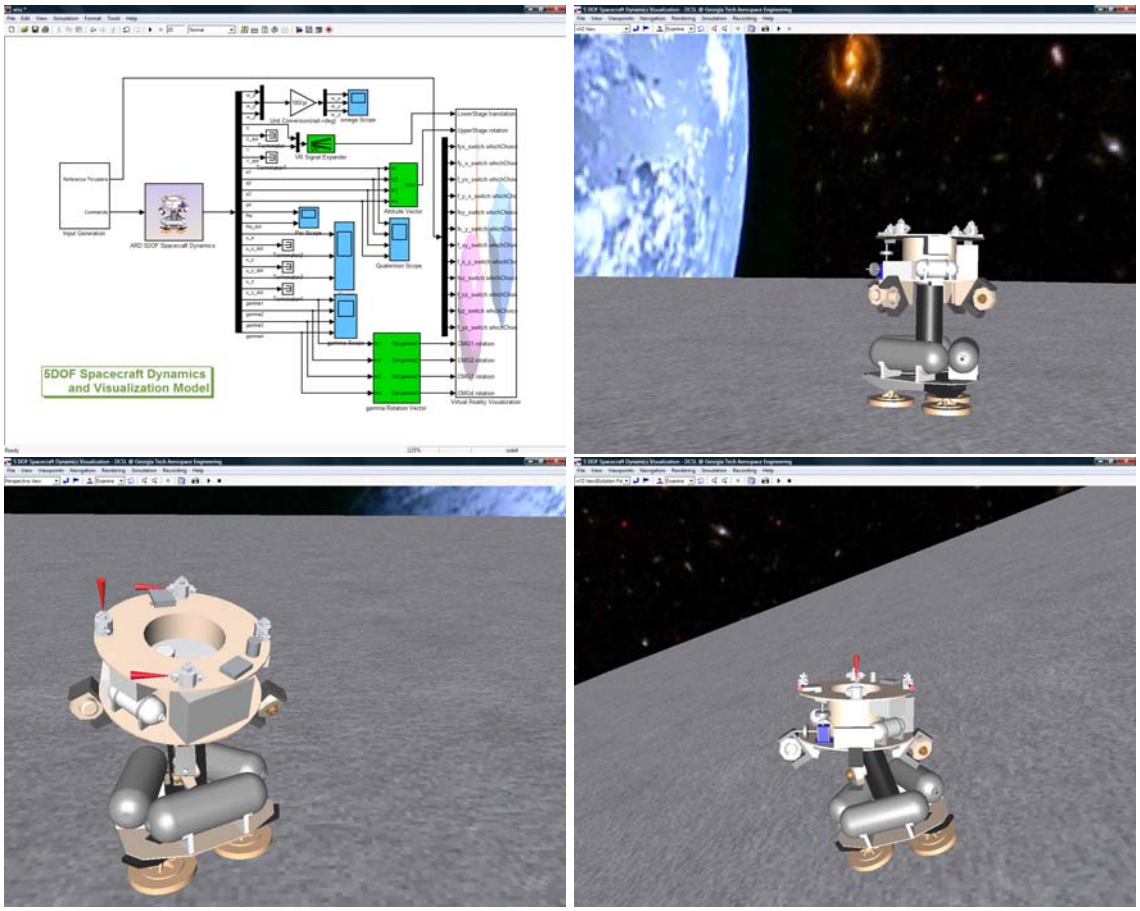


**Figure 12. A Matlab/Simulink model for 5-dof SSARD spacecraft simulation. Several views using the VRML visualization tool are shown.**

on the solution of a linear program. It is assumed that the exact location of each thruster is known and that each thruster has the same thrust level.

Let $\boldsymbol{\tau}_c = [F_x \; F_y \; F_z \; M_x \; M_y \; M_z]^\mathsf{T}$ be the command input to the thruster system, where $F_*$ and $M_*$, $* = (x, y, z)$ denote the desired force and torque commands expressed in the body frame. Let also

$$\boldsymbol{u} = \left[ \begin{array}{cccccccccccc} \boldsymbol{f}_{1p} & \boldsymbol{f}_{1c} & \boldsymbol{f}_{1n} & \boldsymbol{f}_{2p} & \boldsymbol{f}_{2c} & \boldsymbol{f}_{2n} & \boldsymbol{f}_{3p} & \boldsymbol{f}_{3c} & \boldsymbol{f}_{3n} & \boldsymbol{f}_{4p} & \boldsymbol{f}_{4c} & \boldsymbol{f}_{4n} \end{array} \right], \tag{4}$$

be a thruster command vector containing the commands for all 12 thrusters. Notice that $f_{ij} \geq 0$. From the geometry shown in Fig. 11, it is straightforward to formulate a linear mapping from the thruster command $\boldsymbol{u}$ to the force and torque command in body axis as follows,

$$\boldsymbol{\tau}_c = \mathcal{T} \; \boldsymbol{u} \tag{5}$$

where the linear mapping $\mathcal{T}$ is given by

$$\mathcal{T} = \left[ \begin{array}{cccccccccccc} 1 & 0 & -1 & 0 & 0 & 0 & 1 & 0 & -1 & 0 & 0 & 0 \\ 0 & 0 & 0 & 1 & 0 & -1 & 0 & 0 & 0 & 1 & 0 & -1 \\ 0 & 1 & 0 & 0 & 1 & 0 & 0 & 1 & 0 & 0 & 1 & 0 \\ 0 & \ell_h & 0 & \ell_v & 0 & -\ell_v & 0 & -\ell_h & 0 & \ell_v & 0 & -\ell_v \\ -\ell_v & 0 & \ell_v & 0 & -\ell_h & 0 & -\ell_v & 0 & \ell_v & 0 & \ell_h & 0 \\ -\ell_h & 0 & \ell_h & \ell_h & 0 & -\ell_h & \ell_h & 0 & -\ell_h & -\ell_h & 0 & \ell_h \end{array} \right], \tag{6}$$

where $\ell_h$ and $\ell_v$ are the horizontal and vertical distances from the center of rotation to each thrusters.

Suppose that each thruster can generate a force with maximum level $f_{\max}$, i.e. $0 \leq f_{i*} \leq f_{\max}$, $i = 1, \cdots, 4$ and $\star = p, c, n$ where $f_{\max} > 0$ is the maximum thrust level. Note that because no thruster is aligned along the negative $z$-axis, it is impossible to generate negative $z$-axis thrust. Hence, the thrust along the $z$-axis always ends up with $F_z \geq 0$. For this reason, we relax one of the equality constraints in Eq. (5) to an inequality constraint $F_z \geq 0$. Then, the thruster allocation problem is to compute a feasible solution $\boldsymbol{u}$ subject to the force and moment constraints as well as the thruster bounds. We formulate a constrained optimization problem using linear programming as follows,

$$\text{minimize} \quad \boldsymbol{w}^{\mathsf{T}}\boldsymbol{u} \tag{7}$$

where $\boldsymbol{w}$ is a vector of weights, subject to the linear constraints in Eq. (5) and $F_z \geq 0$ and the bounds on the variables

$$0 \leq u_i \leq f_{\max}, \qquad i = 1, \cdots, 12 \tag{8}$$

The previous constrained optimization problem can be efficiently solved using the simplex method. A C++ code was written and implemented as an S-function in the Matlab/Simulink® environment with the help of GNU Linear Programming Kit (GLPK).[15] This S-function environment enables the C++ code to be validated for any errors while being easily incorporated in the current simulation/visualization environment for real-time execution on-board the SSARD.

Figures 13-14 show numerical simulation results from the implementation of the proposed thruster allocation strategy to a simplified model of the SSARD. In the simulation scenario, the attitude is stabilized from a non-zero orientation, while letting the platform move in accordance to open loop translational commands. As shown in Fig. 14(b), two bang-bang commands are employed to move the platform first along the $X$-direction, and then along the $Y$-direction. The results are shown in Figs. 13-14. For the sake of convenience, only the resultant force and moment outputs are plotted instead of each thrust valve output. It should be noted that in the right-bottom plot of Fig. 14(b) a series of bang-bang open-loop force command is generated while the attitude is stabilized by the thrusters. This implies that the thruster allocation algorithm works as expected.

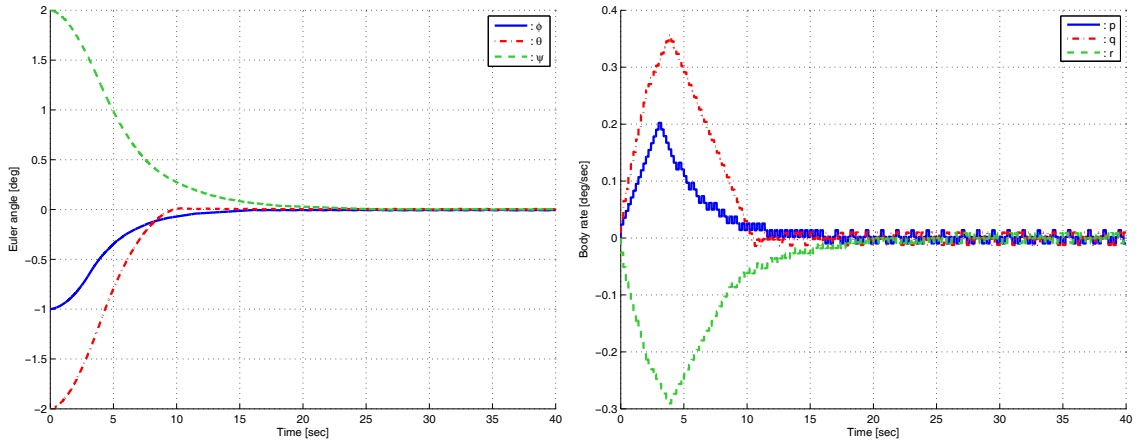


(a) Euler angles (b) Body rates

**Figure 13. Simulation results of both attitude stabilization and translation using thrusters allocation algorithm.**

## VI. Calibration of the Attitude Measurement System Using a Camera/Laser System

### VI.A. Geometry of Vision-Based Attitude Estimation

An attitude estimation algorithm using a stationary, ceiling-mounted vision camera in conjunction with an on-board laser module was developed to calibrate the angular rotation measurements of the platform. The method provides full attitude information of the platform by sensing the laser position and rotation with

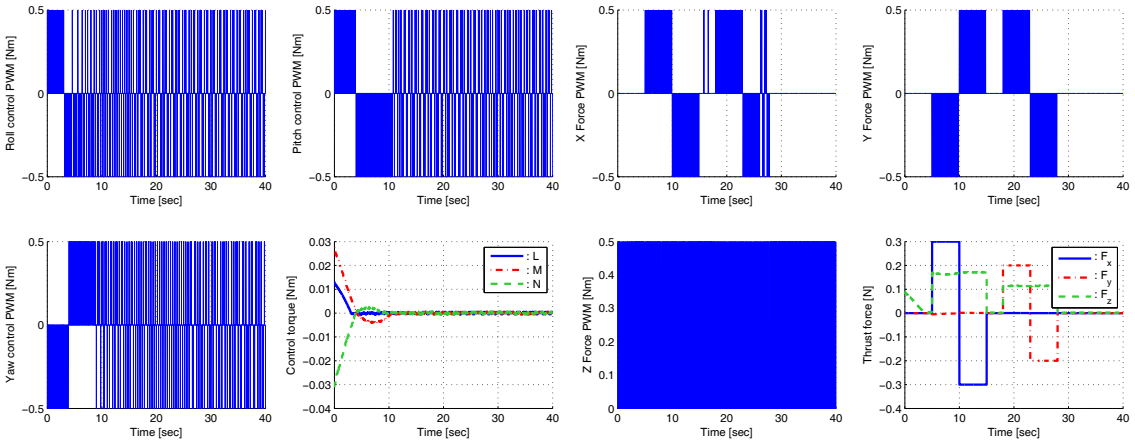


(a) Rotational torque (b) Translational force

**Figure 14. Control commands for attitude stabilization and translation using thruster allocation algorithm.**

respect to the target plane using the ceiling-mounted camera. The algorithm also compensates for the heading angle bias/drift of the magnetometer measurements resulting from spurious environmental electro-magnetic disturbances. Such disturbances deteriorate the IMU sensor measurements. The proposed algorithm provides a way to improve accuracy of the attitude estimation by providing drift-free results.

The overall schematic is shown in Figs. 15 and 16. We assume that the laser module is rigidly attached to the spacecraft platform. The laser projects a cross-shaped image onto the target plane, while an external camera captures the cross shape on the target plane. As illustrated in Fig. 16, the laser beam falls onto the target plane forming a tilted cross shape with the intersection point $(x_t, y_t)$ and the associated slope $m = \tan\phi_t$. The overhead camera is assumed to be coplanar with the center of rotation of the SSARD and the target origin. In Fig. 15 three frames of reference are shown, representing the geometry of the problem: The inertial frame, located at the center of rotation of the whole platform denoted by $\mathcal{I} = (\hat{I}, \hat{J}, \hat{K})$, the target frame denoted by $\mathcal{T} = (\hat{\mathbf{t}}_\mathbf{1}, \hat{\mathbf{t}}_\mathbf{2}, \hat{\mathbf{t}}_\mathbf{3})$, and the camera frame denoted by $\mathcal{C} = (\hat{\mathbf{c}}_\mathbf{1}, \hat{\mathbf{c}}_\mathbf{2}, \hat{\mathbf{c}}_\mathbf{3})$. The positive $z$-axis with respect to the camera frame $(\mathcal{C})$ is directed towards the center of the target frame. A simple pin-hole camera model is utilized, although the image plane is assumed to be located at the positive $z$-direction to cope with the actual non-inverting images from the camera.

Let $\mathcal{R}_{tc}$ be the rotation matrix from the camera frame to the target frame, and suppose $\theta_c$ is the camera inclination angle defined by the unit vectors $\hat{\mathbf{c}}_\mathbf{3}$ and $\hat{I}$. Let $[x_t, y_t, z_t]^\mathsf{T}$ and $[x_c, y_c, z_c]^\mathsf{T}$ represent the coordinates of the laser cross point expressed in the target frame and the camera frame, respectively. From the pinhole camera model[16] we may calculate the coordinates of the center point of the cross on the image plane as follows,

$$\begin{bmatrix} I_x \\ I_y \\ 1 \end{bmatrix} = \begin{bmatrix} \alpha_u & -\alpha_u \cot\gamma & u_0 \\ 0 & \alpha_v \csc\gamma & v_0 \\ 0 & 0 & 1 \end{bmatrix} \begin{bmatrix} x_c/z_c \\ y_c/z_c \\ 1 \end{bmatrix} \triangleq \mathcal{K} \begin{bmatrix} x_c/z_c \\ y_c/z_c \\ 1 \end{bmatrix} \tag{9}$$

where $\mathcal{K}$ is a nonsingular $3 \times 3$ upper triangular matrix known as the camera calibration matrix.[16] The five parameters of the matrix $\mathcal{K}$ are the focal length $f$, the horizontal pixel number per unit distance $k_u$, the vertical pixel number per unit distance $k_v$, $\alpha_u = k_u f, \alpha_v = k_v f$, and the principal point on the image plane $(u_0, v_0)$, which is the point where the optic axis intersects the image plane. We assume the camera coordinate skew angle $\gamma_c$ to be 90 deg, which implies the orthogonality of each coordinate of the camera frame.

The coordinates of the cross origin in terms of the target frame is obtained by the following affine

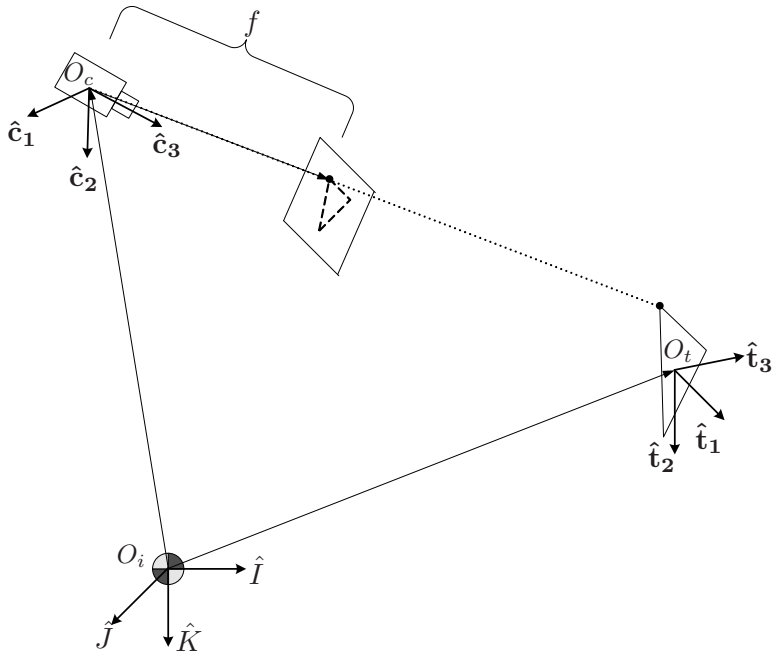


**Figure 15. Schematic for three kinds frames and a pin hole camera model.**

transformation

$$\begin{bmatrix} x_t \\ y_t \\ z_t \end{bmatrix} = \mathcal{R}_{tc} \begin{bmatrix} x_c \\ y_c \\ z_c \end{bmatrix} + \mathbf{t}, \tag{10}$$

where $\mathbf{t}$ denotes the coordinate of the target frame's origin. Substituting Eq. (9) into Eq. (10), we can relate the laser cross point in the target frame with the one in the image plane by

$$\begin{bmatrix} x_t \\ y_t \\ z_t \end{bmatrix} = \mathcal{R}_{tc}\mathcal{K}^{-1} z_c \begin{bmatrix} I_x \\ I_y \\ 1 \end{bmatrix} + \mathbf{t}. \tag{11}$$

Let now $L$ be the horizontal distance between the origin of frame $\mathcal{I}$ and frame $\mathcal{T}$, and let also $L_c$ and H be the horizontal and vertical distances between the origins of the frames $\mathcal{I}$ and $\mathcal{C}$, respectively. From the assumption about the camera location, it follows that the coordinate of the target origin is given by $\mathbf{t} = [0$ -H -(L-$L_c$)$]^{\mathsf{T}}$. Note that $z_t$ is always zero because the laser beam is projected on the wall. It follows that Eq. (11) ends up with the following form:

$$\begin{bmatrix} x_t \\ y_t \end{bmatrix} = \begin{bmatrix} \alpha_u & -(I_x - u_0)\mathrm{s}\theta_c \\ 0 & \alpha_v \mathrm{c}\theta_c - (I_y - v_0)\mathrm{s}\theta_c \end{bmatrix}^{-1} \begin{bmatrix} I_x - u_0 & 0 \\ I_y - v_0 & \alpha_v \end{bmatrix} \begin{bmatrix} \mathrm{c}\theta_c & -\mathrm{s}\theta_c \\ \mathrm{s}\theta_c & \mathrm{c}\theta_c \end{bmatrix} \begin{bmatrix} L - L_c \\ -H \end{bmatrix}, \tag{12}$$

whose solution is uniquely determined if $\alpha_v \mathrm{c}\theta_c - (I_y - v_0)\sin\theta_c \neq 0$. If the light ray becomes parallel to the target $\hat{\mathbf{t}}_1 - \hat{\mathbf{t}}_2$ plane, then no unique solution exists.

From trigonometry, it is straightforward to obtain explicit expressions relating the coordinate of the point $A$ in the target frame with the attitude angles $\theta$ and $\psi$, as follows

$$\tan\psi = \frac{x_t}{L}, \tag{13}$$

and

$$\tan\theta = -\frac{y_t}{\sqrt{L^2 + x_t^2}}, \tag{14}$$

where we have assumed a conventional 3($\psi$)-2($\theta$)-1($\phi$) rotational sequence and $|\psi|, |\theta| < 90$ [deg].

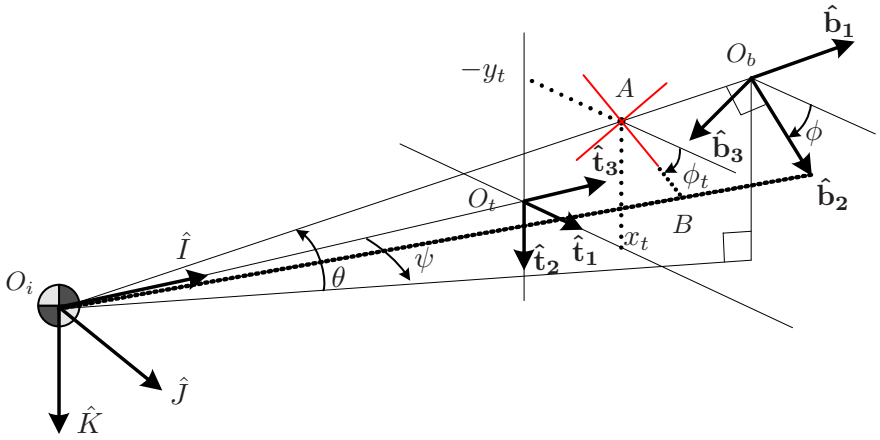


**Figure 16. Projection of the cross laser beam onto the target plane. The center of cross falls on the point $A$ and the cross beam forms an rotational angle $\phi_t$ with respect to $\hat{\mathbf{t}}_1$.**

Since the cross of the laser beam is projected on the $\hat{\mathbf{t}}_1 - \hat{\mathbf{t}}_2$ plane, it should be noted that the line $\overrightarrow{AB}$ is the common line of two planes whose normal vectors are $\hat{\mathbf{b}}_3$ and $\hat{\mathbf{t}}_3$. It follows that $\hat{\mathbf{b}}_3$ can be calculated from

$$\hat{\mathbf{b}}_3 = \begin{bmatrix} \mathrm{c}\psi\mathrm{s}\theta\mathrm{c}\phi + \mathrm{s}\psi\mathrm{s}\phi \\ \mathrm{s}\psi\mathrm{s}\theta\mathrm{c}\phi - \mathrm{c}\psi\mathrm{s}\phi \\ \mathrm{c}\theta\mathrm{c}\phi \end{bmatrix}.$$

Suppose now that the target frame is inertially fixed and that $\hat{I}$ is parallel to $\hat{\mathbf{t}}_3$. Then the normalized direction vector of $\overrightarrow{AB}$ can be obtained by the cross product of two vectors as follows,

$$\frac{\overrightarrow{AB}}{\|\overrightarrow{AB}\|} = \hat{\mathbf{t}}_3 \times \hat{\mathbf{b}}_3 = \begin{bmatrix} -\mathrm{c}\theta\mathrm{c}\phi \\ \mathrm{s}\psi\mathrm{s}\theta\mathrm{c}\phi - \mathrm{c}\psi\mathrm{s}\phi \\ 0 \end{bmatrix}.$$

The slope of $\overrightarrow{AB}$ in $\hat{\mathbf{t}}_1 - \hat{\mathbf{t}}_2$ plane is calculated as follows,

$$m = \frac{\mathrm{c}\psi\mathrm{s}\phi - \mathrm{s}\psi\mathrm{s}\theta\mathrm{c}\phi}{\mathrm{c}\theta\mathrm{c}\phi}. \tag{15}$$

By solving Eq. (15) for $\phi$, we can get the following formula to compute $\phi$ from the projected coordinate and the slope of the laser beam with respect to the target frame

$$\tan\phi = \frac{(L^2 + x_t^2)m - x_t y_t}{L\sqrt{L^2 + x_t^2 + y_t^2}}. \tag{16}$$

### VI.B. Sensitivity Analysis

Even though the formulas in Eqs. (13), (14), (16) are the exact solutions that give the Euler angles of the upper stage of the platform in terms of the camera measurements, the results may still be inaccurate owing to uncertainties in the problem parameters such as the location/alignment of the camera, the laser beam, the target, etc. We may obtain the best estimates of these parameters during the initial calibration process, however, there still exists the possibility of using inexact parameters in the angle estimation algorithm. In light of these issues, it is important to ascertain the robustness of the estimation algorithm under such uncertainties. We have thus conducted a Monte Carlo simulation using the parameter uncertainties within given bounds. Specifically, we assumed that the camera and the target have position uncertainties corresponding to a normal distribution with 1-$\sigma$ values given by $[0.1,\ 0.01,\ 0.01]^{\mathsf{T}}$ and $[0.1,\ 0.01,\ 0.1]^{\mathsf{T}}$ meters, respectively.

Figure 17 shows the results from the Monte Carlo simulation for different baselengths $L = 3, 5, 10$ meters. Each plot shows that the performance of the estimation algorithm increases with increasing baselength, as expected. The standard deviations of the estimation error are summarized in Table 1 and are deemed acceptable. Note that these results refer to absolute measurement errors. The relative angle measurement errors are expected to be even smaller.

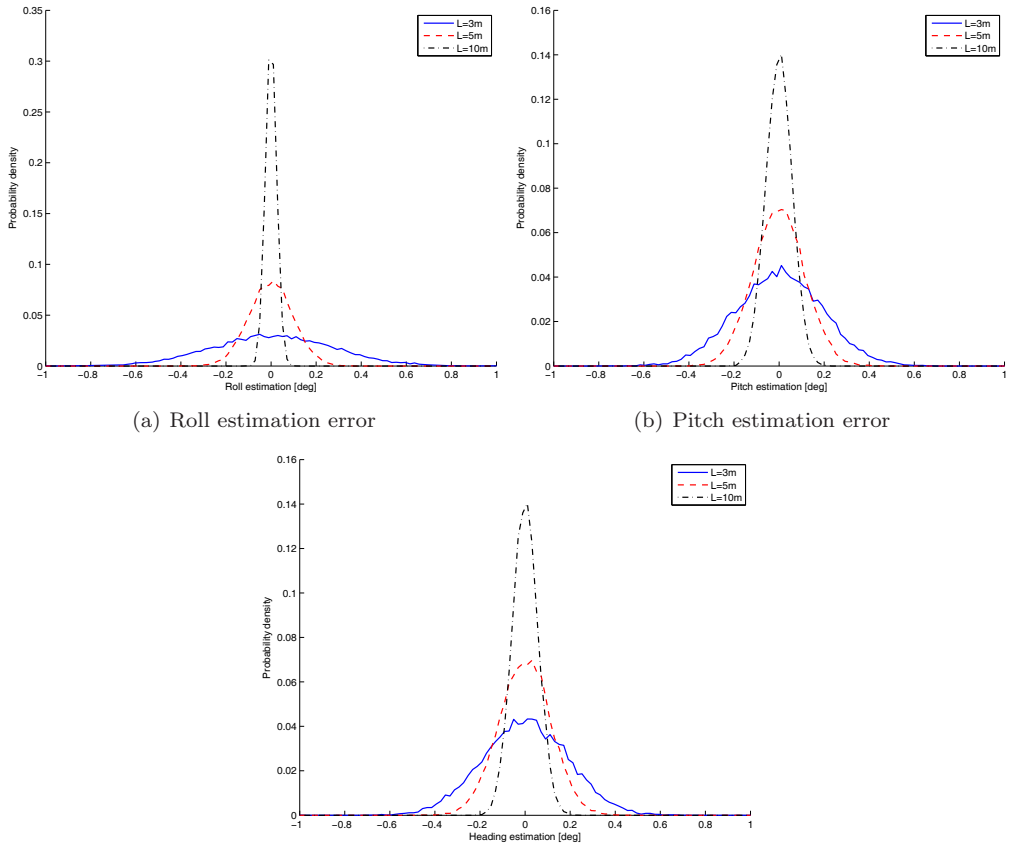


(a) Roll estimation error

(b) Pitch estimation error

(c) Heading estimation error

**Figure 17. Monte Carlo simulation test for robustness of the angle estimation algorithm under bounded uncertainties.**

## VI.C. Calibration and Implementation

The calibration process requires estimating the calibration matrix $\mathcal{K}$ for the unknown parameters $x = [\alpha_u, \alpha_v, u_0, v_0]^\mathsf{T}$. We let $y = [I_x, I_y]^\mathsf{T}$ be the measurement vector for the 16 sample points on the image plane, whose actual locations are known a priori (see Fig. 18). Then, if we rearrange Eq. (12) by placing the unknown parameters on the right hand side and the measurements on the left side, Eq. (12) collapses to the simple regression form $y = \mathcal{A}x$ with $\mathcal{A}$ being a regressor matrix. In order to estimate the unknown parameters, we use least-squares, that is, we solve the minimization problem

$$\min_x \|y - \mathcal{A}x\|_2.$$

This calibration process eliminates the persistent estimation error due to the misalignment of the camera and the target with respect to the inertial frame, since both the target and the camera do not change their orientation and position after initial installation. The calibration was done using the following values $L$=50.55, $L_c$=6.10, $H_c$=17.02 [meters]. Table 2 summarizes the results of the calibration process with the average values and the 1-$\sigma$ variation. From the results, it can be inferred that the principal point $(u_0, v_0)$ is closely located at the center of the image (of size 640×480 pixels), and is less sensitive to estimation error. However, the estimation results for $\alpha_u$ and $\alpha_v$ (horizontal and vertical focal length of the lens) show that

**Table 1. Estimation errors from Monte Carlo simulation.**

| Angle | Mean | 1-$\sigma$ | Units |
|---|---|---|---|
| $L$=3 meters | | | |
| Roll $\phi$ | 0.0054 | 0.2721 | deg |
| Pitch $\theta$ | 0.0011 | 0.1919 | deg |
| Heading $\psi$ | 0.0006 | 0.1902 | deg |
| $L$=5 meters | | | |
| Roll $\phi$ | -0.00051 | 0.0972 | deg |
| Pitch $\theta$ | -0.00083 | 0.1136 | deg |
| Heading $\psi$ | -0.0006 | 0.1145 | deg |
| $L$=10 meters | | | |
| Roll $\phi$ | -0.00066 | 0.0242 | deg |
| Pitch $\theta$ | -0.00066 | 0.0575 | deg |
| Heading $\psi$ | -0.00006 | 0.0572 | deg |

the lens of the camera introduces a bit of distortion. As a result, for better results it is recommended to use a lookup table to select the appropriate values of $\alpha_u$ and $\alpha_v$ in accordance with the identified center pixel location. Nonetheless, in this paper we used the estimated values of $\alpha_u$ and $\alpha_v$ for the sake of convenience.

The algorithm was implemented in a Visual C++ environment in conjunction with the OpenCV library. The captured image is thresholded, and then a Hough transform is applied to locate the two lines, after which the previous algorithm is applied to derive the Eulerian angles. The algorithm was implemented at the same rate as the camera frame per rate, 30 [fps], on an Intel(R) Core 2 CPU at 2.66GHz PC computer.

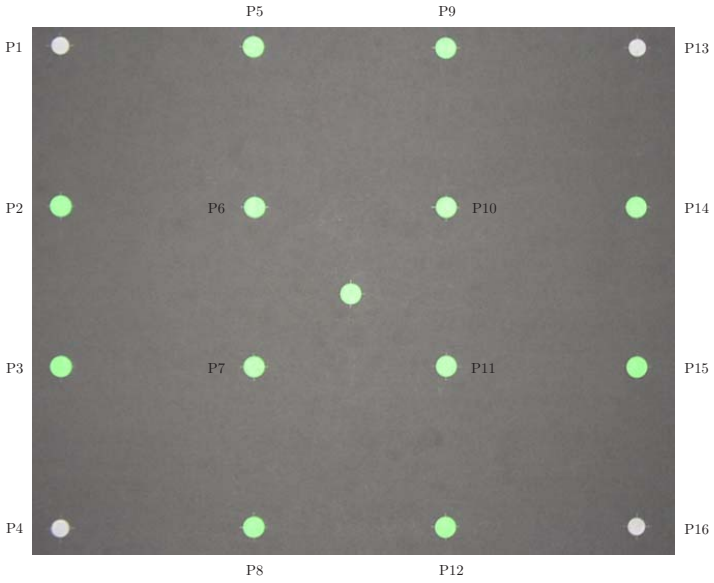


**Figure 18. Target view from spacecraft horizon.**

## VII. Summary and Conclusions

Autonomous proximity operations, including the capability for timely, on-demand, on-orbit servicing and refueling of space assets, have long been deemed as an enabling factor enhancing current space operational

**Table 2. Estimated parameters and their statistics (in pixels)**

| | $u_0$ | $v_0$ | $\alpha_u$ | $\alpha_v$ |
|---|---|---|---|---|
| Average | 313.88 | 246.98 | 5090.6 | 4998.8 |
| 1-$\sigma$ | 0.4964 | 0.6232 | 22.0955 | 34.4681 |

capabilities both in the military and the civilian sectors. Realistic validation and testing of ARD technology is a first crucial step before such technology is incorporated in future spacecraft. Unfortunately, there are only a few experimental facilities that can be used to test new ARD technology, especially in an academic environment. In this paper we describe a new 5-dof experimental facility for autonomous rendezvous and docking of spacecraft at the Dynamics and Control Systems Laboratory at the School of Aerospace Engineering at Georgia Tech. This 5-dof Spacecraft Simulator platform for Autonomous Rendezvous and Docking (SSARD) incorporates a diverse collection of sensors and actuators, allowing great flexibility for performing experiments under a variety of realistic conditions. The 5-dof SSARD is a unique research and educational experimental facility among US academic institutions, which will enable unprecedented, realistic testing of new rendezvous and docking control algorithms and hardware.

### Acknowledgment

This work has been supported by AFOSR DURIP award no. FA9550-06-1-0379 and a contract from SAIC.

## References

[1]Iannotta, B., "SUMO Wrestles Satellites into New Orbits," *Aerospace America*, Vol. 2, Feb. 2006, pp. 26–30.

[2]Hollander, S., "Autonomous Space Robotics: Enabling Technologies for Advanced Space Platforms," *Space 2000 Conference and Exposition*, Long Beach, CA, 2000, AIAA Pager 00-5079.

[3]Gogan, L., Melko, J., Wang, F., Lourme, D., Moha, S. B., Largon, C., and Richard, M., "Manned Mission to Mars with Periodic Refueling from Electrically Propelled Tankers," *Proceedings of the 8th Annual Summer Conference: NASA/USRA Advanced Design Program*, 1994, pp. 22–30.

[4]Koelle, D. E. and Obersteiner, M., "Orbital Transfer Systems for Lunar Missions," *The 42th International Astronautical Congress*, Montreal, Canada, Oct. 1991.

[5]Koelle, D. E. and Koelle, H. H., "Lunar Space Transportation System Options," *The 47th International Astronautical Congress*, Beijing, China, Oct. 1996.

[6]"Orbital Issues DART Mission Recap," April 2005, http://www.orbital.com/NewsInfo/release.asp?prid=500.

[7]Romano, M., "On-the-ground Axperiments of Autonomous Spacecraft Proximity-Navigation using Computer Vision and Jet Actuators," *IEEE/ASME International Conference of Advanced Intelligent Mechatronics*, Monterey, CA, July 2005.

[8]Romano, M., "Laboratory Experimentation of Autonomous Spacecraft Proximity-Navigation using Vision and Inertia Sensors," *AIAA Guidance, Navigation, and Control Conference and Exhibit*, San Francisco, CA, 2005.

[9]Jung, D. and Tsiotras, P., "A 3-DoF Experimental Test-Bed for Integrated Attitude Dynamics and Control Research," *AIAA Guidance, Navigation, and Control Conference*, Austin, Texas, 2003, AIAA 2003-5331.

[10]Jung, D. and Tsiotras, P., "An Experimental Comparison of CMG Steering Control Laws," *AIAA/AAS Astrodynamics Specialist Conference and Exhibit*, Providence, RI, 2004, AIAA Paper 2004-5294.

[11]Kim, B., Velenis, E., Kriengsiri, P., and Tsiotras, P., "A Low-Cost Spacecraft Simulator For Research And Education," *IEEE Control Systems Magazine*, 2002, to appear.

[12]Schwartz, J. L., Peck, M. A., and Hall, C. D., "Historical Review of Air-Bearing Spacecraft Simulators," *Journal of Guidance, Control, and Dynamics*, Vol. 26, No. 4, 2003, pp. 513–522.

[13]Garus, J., "Optimization of Thrust Allocation in the Propulsion System of an Underwater Vehicle," *International Journal of Applied Mathematics and Computer Sciences*, Vol. 14, No. 4, 2004, pp. 461–467.

[14]Servidia, P. A. and Pea, R. S., "Spacecraft Thruster Control Allocation Problems," *IEEE Transactions on Automatic Control*, Vol. 50, No. 2, Feb. 2005, pp. 245–249.

[15]Makhorin, A., "GNU Linear Programming Kit," Electronic, http://www.gnu.org/software/glpk/.

[16]Forsyth, D. and Ponce, J., *Computer Vision: A Modern Approach*, Prentice Hall, 2003.